

Six-Degree-of-Freedom Steerable Visible-Light-Driven Microsubmarines Using Water as a Fuel: Application for Explosives Decontamination

Yulong Ying, Jan Plutnar, and Martin Pumera*

Micro/nanomotors are capable of a wide variety of tasks related, i.e., to biomedical or environmental applications. Light-driven semiconductor-based micromotors are especially appealing, as they can split surrounding water via light irradiation, and therefore, they can move infinitely. However, their motion is typically limited to in-plane motion with four degrees of freedom (4DoF) or even pseudo-1D motion with 2DoF. Herein, magnetically steerable tubular $\text{TiO}_2/\text{Fe}_3\text{O}_4/\text{CdS}$ micromotors, termed microsubmarines, with 6DoF motion, based on a fuel-free design where surrounding water acts as fuel upon visible light irradiation, are presented, with an average velocity of $7.9 \mu\text{m s}^{-1}$. Besides, the generation of radicals via such water splitting aids the photocatalytic chemicals degradation with the potential to use solar radiation. A light-induced self-electrophoretic mechanism is responsible for the self-propulsion and can be used to predict the motion direction based on the structure and composition. Finally, the $\text{TiO}_2/\text{Fe}_3\text{O}_4/\text{CdS}$ microsubmarines are tested in a proof-of-concept application of high-energy explosive, e.g., picric acid, photocatalytic degradation, with the best performance owing to the versatility of 6DoF motion, the surface coating with amorphous TiO_2 layer, and UV light. The results can help optimize light-active micromotor design for potential national security and environmental application, hydrogen evolution, and target cargo delivery.

vest and convert light energy into mechanical motion.^[1] The light source could be easily integrated into the target system, such as the bio-applications or water remediation system, enabling the remote control of the movement and precise tuning of the speed.^[2] Recently, light-driven MNMs are especially appealing in the photocatalytic pollutant degradation owing to the combination of motion-induced mixing enhancement and their intrinsic catalytic characters.^[3,4] More importantly, the potential use of solar radiation as the energy source to drive the movement of MNMs and for environmental remediation makes it the most attractive self-sustainable technology of the future.^[5]

According to the nature of the photoactive materials and the light-matter interaction, there are five most essential MNMs driving mechanisms known to date, i.e., photochromic molecular structure change, photothermal heating, photosensitive decomposition, photocatalytic reaction, and photon momentum transfer/optical forces.^[5–9] Among them, incorporating

photocatalysts into the micromotors structure is the primary strategy to construct light-driven MNMs. An asymmetric shape or composition of such MNMs is necessary to initiate their propulsion as a result of a photocatalytic products' gradient buildup

1. Introduction

Light-driven micro/nanomachines (MNMs) are photoactive materials-based small-sized synthetic devices, which could har-

Dr. Y. Ying, Dr. J. Plutnar, Prof. M. Pumera
Center for the Advanced Functional Nanorobots
Department of Inorganic Chemistry
University of Chemistry and Technology
Technická 5, Prague 16628, Czech Republic
E-mail: pumera.research@gmail.com

Prof. M. Pumera
Future Energy and Innovation Laboratory
Central European Institute of Technology
Brno University of Technology
Purkyňova 123, Brno 61200, Czech Republic

 The ORCID identification number(s) for the author(s) of this article can be found under <https://doi.org/10.1002/smll.202100294>.

© 2021 The Authors. Small published by Wiley-VCH GmbH. This is an open access article under the terms of the Creative Commons Attribution-NonCommercial-NoDerivs License, which permits use and distribution in any medium, provided the original work is properly cited, the use is non-commercial and no modifications or adaptations are made.

Prof. M. Pumera
Department of Chemistry and Biochemistry
Mendel University in Brno
Zemědělská 1, CZ, Brno 61300, Czech Republic
Prof. M. Pumera
Department of Chemical and Biomolecular Engineering
Yonsei University
50 Yonsei-ro, Seodaemun-gu, Seoul 03722, Korea
Prof. M. Pumera
Department of Medical Research
China Medical University Hospital
China Medical University
No. 91 Hsueh-Shih Road, Taichung 40402, Taiwan

DOI: 10.1002/smll.202100294

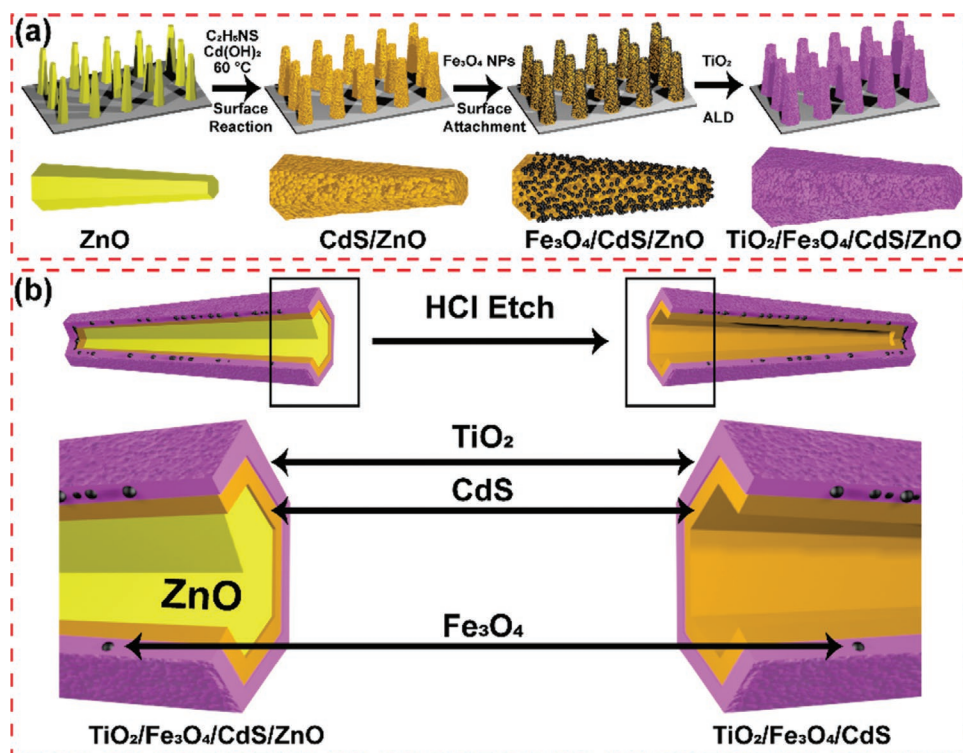
(e.g., Janus type or tubular shape).^[10] Among the photoactive materials used in constructing the light-driven MNMs, TiO₂,^[11] BiOI,^[12] BiVO₄,^[13] Cu₂O/Au,^[14] ZnO/Pt,^[15–17] g-C₃N₄,^[18] CoO,^[19] and AgCl^[20] are the most frequently used semiconducting photocatalysts owing to their fast photoresponse and stability. The majority part of the radiant energy of the sun is spread in the range 250–2500 nm, composed of visible light (44%), infrared light (53%), and ultraviolet (UV, 3%) after considering the scattering and filtering through Earth's atmosphere.^[21,22] Recently, it is still a challenge in the design of water-fueled photoactive micromachines using the visible part of the solar spectrum and with a sufficient motion capability. Most of the current light-driven MNMs are active only under UV irradiation.^[11,15–17] Some of them could be active under visible light but require additional fuels (mainly H₂O₂) and/or a presence of a noble metal (Pt, Au) to propel them.^[13,14,18] The utilization of visible light is crucial in designing light-driven MNMs for future practical environmental remediation applications. Apart from their limited speed, UV light dependence, and fuel dependence, most of the current semiconductor-based MNMs are challenged by the reality that they settle to the bottom with four degrees of freedom (4DoF) movement because of their high density and solid body, which significantly suppresses their motion-induced enhancement of fluid mixing.^[23,24] Hence, it is necessary to redesign the visible-light-driven MNMs in composition and structure to maximize their light-response activity and motion ability (from 4DoF to 6DoF) to extend their applications.

Owing to its chemical stability, low cost, and nontoxicity, titanium dioxide (TiO₂) is an ideal photocatalyst but only responds to the UV radiation due to the relatively high bandgap value (3.0–3.2 eV).^[25] Cadmium sulfide (CdS) is one of the most visible-light-active semiconductors with a direct bandgap (≈2.4 eV) and widely used as a sensitizer to strengthen the charge carrier transfer and improve the light absorption capability.^[26] The coupling of CdS with TiO₂ would directly extend their light activity to the visible region. Meanwhile, the vertically aligned ZnO arrays on a substrate could be well used as a sacrificial template to construct tubular CdS structure for the design of low-weight MNM body,^[16] where the solubility constant (*K*_{sp}) difference-induced ions exchange provides a mild approach to convert dynamically single component (ZnO) to bi-component core-shell structure (CdS/ZnO).^[27,28] In this work, we designed magnetically controllable photocatalytic tubular TiO₂/Fe₃O₄/CdS micros submarines, which show fast 6DoF movement under visible light irradiation in the absence of any additional fuels. It is the first time that a tubular CdS/Fe₃O₄/TiO₂ core-shell structure was used to construct visible-light-driven micromotors. The motion mechanism was studied by comparison of micromotors with variable composition, i.e., CdS/ZnO, TiO₂/Fe₃O₄/CdS/ZnO, and TiO₂/Fe₃O₄/CdS. The tightly embedded Fe₃O₄ nanoparticles (NPs) between the interfaces of TiO₂/CdS endow the micros submarines with controllable manipulation under an external magnetic field, i.e., rotation and navigation. These CdS-based micromotors were used to degrade the nitroaromatic explosives and dye pollutants under visible- and UV light irradiation, where the TiO₂/Fe₃O₄/CdS micros submarines presented the best efficiency due to the particular 6DoF motion behavior and specific composition of α-TiO₂. Our findings promote a better understanding of the photophoretic mechanism and suggest the future direction in optimizing the design of the light-active micromotors for potential national security and environmental application.

2. Results and Discussion

2.1. Preparation and Characterization of CdS-Based Micromotors

The tubular TiO₂/Fe₃O₄/CdS micros submarines were prepared through five main steps: 1) Hydrothermal growth of vertically aligned ZnO arrays on a silicon substrate; 2) a two-step successive ion-exchange reaction for the synthesis of CdS/ZnO structure; 3) surface anchoring of Fe₃O₄ NPs on CdS/ZnO; 4) atomic layer deposition (ALD) of TiO₂ layer on the top surface; 5) detachment from the substrate and subsequent etching of the inner ZnO by HCl, as shown in **Scheme 1** (experiment detailed in the Supporting Information). Scanning electron microscopy (SEM), energy-dispersive X-ray spectroscopy (EDS), scanning transmission electron microscopy (STEM), and X-ray diffractometry (XRD) were performed to characterize the structure, composition, and crystallinity. Figure S1 (Supporting Information) showed the shape and size distribution of the hydrothermally grown ZnO arrays on the surface of a silicon wafer, 500 nm to 1 μm in diameter and 8 μm in length. Besides, the top side's diameter is a little smaller than its bottom side, according to the SEM results. The XRD pattern of the ZnO microrods in Figure S2 (Supporting Information) showed the characteristic diffractions corresponding to the hexagonal wurtzite structure (JCPDS PDF No. 36-1451). In the process of two-step successive ion-exchange with S²⁻ and Cd²⁺, the sample on the silicon wafer's surface turned yellow. The material was subsequently annealed at 550 °C under Ar atmosphere. Besides the color change, the presence of the CdS layer on the surface of the ZnO microrods was confirmed by the XRD (Figure S2, Supporting Information), where a new set of diffraction peaks corresponding to the hexagonal wurtzite phase of CdS (JCPDS PDF No. 41-1049) was detected. Figure S3a–d (Supporting Information) shows the presence of the CdS layer on the ZnO microrods in different magnifications. It is clearly demonstrated that the surface of the microrods was fully covered by a new layer during the ion exchange reactions (Figure S3a, Supporting Information). The newly formed CdS layer (25 nm thick) consists of numerous intergrown crystals (≈20 nm, Figure S3b–d, Supporting Information). The EDS analysis (Figure S3e, Supporting Information) shows a homogeneous distribution of Zn (15 at%), Cd (12 at%), S (12 at%), and O (61 at%) and a distinct boundary between the CdS and ZnO layer at the bottom end of the rod (solid white circle in Figure S3e, Supporting Information), originally attached to the surface of the silicon wafer. Subsequently, a homogeneous TiO₂ layer was deposited on the surface by the ALD technique and controlled to be around 100 nm thickness. The surface turned out to be smooth again (Figure S4a, Supporting Information), and the presence of Ti (11 at%) is confirmed by the high-resolution EDS (HR-EDS) mapping (Figure S4b, Supporting Information), co-existing with Cd (6 at%), S (5 at%), Zn (28 at%), and O (50 at%). The multilayer structure of TiO₂/CdS/ZnO could be distinguished, where Zn is mainly located in the middle of the structure while Ti, Cd, and S have a broader distribution. The bottom end boundary is apparent, where Zn is in the core, Ti is in the shell layer, and Cd is in the middle layer. No additional peaks were observed in the corresponding XRD spectrum (Figure S1, Supporting Information), indicating the amorphous structure of TiO₂



Scheme 1. Schematic illustrations on the design of the CdS-based micros submarines. a) Step processes involved in the hydrothermal growth of ZnO arrays, successive ion-exchange reaction for the synthesis of CdS layer, surface attachment of Fe₃O₄ NPs, and ALD deposition of TiO₂ layer. b) Schematic step of ZnO etching in preparation of TiO₂/Fe₃O₄/CdS micros submarines and their high-resolution layer structure.

(α -TiO₂). Later, the magnetic Fe₃O₄ NPs were also incorporated onto the surface of CdS/ZnO by surface attachment, resulting in TiO₂/Fe₃O₄/CdS/ZnO following by ALD deposition of TiO₂. However, no characteristic element Fe signal and additional peaks associated with Fe₃O₄ NPs were detected from the TiO₂/Fe₃O₄/CdS/ZnO sample by the SEM-EDS and XRD, respectively (Figure S2, Supporting Information) due to low concentrations of the nanoparticles. Hence, the existence of Fe₃O₄ NPs was demonstrated by the magnetic manipulation experiment.

The ZnO core was completely etched using HCl, and a tubular TiO₂/CdS double-layer structure was obtained. A perfect one-end open tubular structure with a wall thickness around 100 nm was isolated after etching treatment, as shown in Figure 1 and Figure S5 (Supporting Information). HR-EDS mappings (Figure 1e) indicated the effective etching of ZnO (0 at%) and preservation of the TiO₂ (11 at%) and CdS (8–12 at%) layers. The etching progress was also recorded for the samples with a shorter etching time (Figure S6, Supporting Information).

2.2. Motion Analysis of CdS-Based Micros submarines under Visible Light

ZnO and TiO₂ are two of the most commonly used n-type metal oxide semiconductors with quite similar physicochemical properties, i.e., bandgap (\approx 3.2 eV), light absorption properties (near-ultraviolet region), and conduction band (CB) and valence

band (VB) position.^[29–31] Both of them have been widely used as photocatalysts owing to their low cost, high abundance, high activity, and nontoxicity. It has been demonstrated that pristine ZnO micromotors only showed a very weak Brownian motion behavior even under UV light irradiation in pure water due to their high density and low carriers separation efficiency, while they could present a nearly circular motion when asymmetrically coated with Pt and exposed to UV light.^[16] Under visible light irradiation, the light-driven motion could not occur based on the material's light absorption ability. To realize the potential visible-light activation, we introduced the widely used visible-light-active semiconductor (CdS) to construct a heterojunction enhancing the visible light absorption and carrier separation efficiency.

The light-driven motion behavior of these CdS-based micros submarines (CdS/ZnO, TiO₂/Fe₃O₄/CdS/ZnO, and TiO₂/Fe₃O₄/CdS) was studied in pure water under the external visible light irradiation in the absence of any additional fuels (Figure 2 and Videos S1–S3, Supporting Information). The UV region (below 400 nm) from the external xenon (Xe) lamp was filtered using a UV-cut filter cube. In the absence of external Xe light, both CdS/ZnO and TiO₂/Fe₃O₄/CdS/ZnO micromotors only showed a minimal displacement in pure water due to the Brownian motion, heavy mass, and weak light intensity from internal optical microscopy (Videos S1 and S2, Supporting Information). In contrast, a directional movement was observed for the tubular TiO₂/Fe₃O₄/CdS micros submarines even when illuminated by the weak light from internal optical microscopy only (Video S3, Supporting Information). It is suggested that the

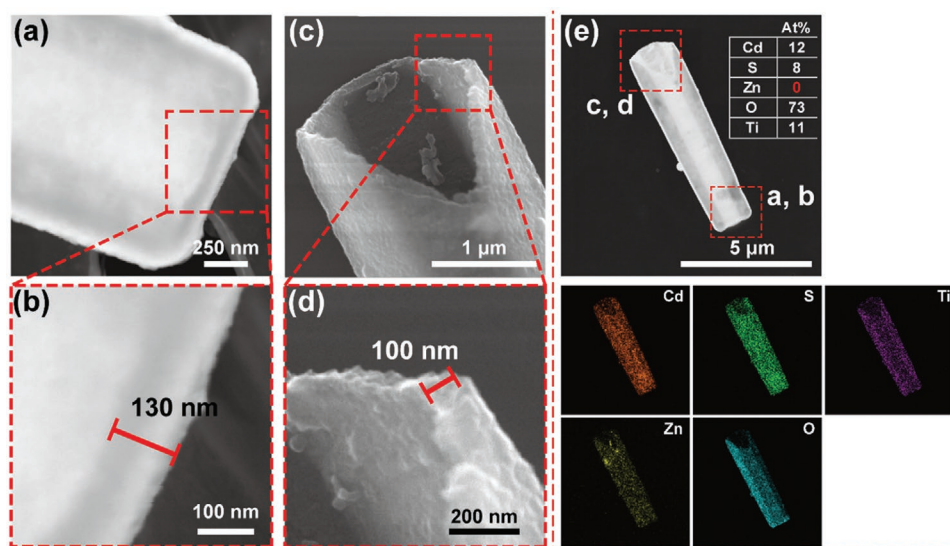


Figure 1. STEM characterizations and HR-EDS images of TiO_2/CdS micros submarines. a, c) Enlarged STEM images of micros submarine in (e). b, d) Wall thickness at both ends. e) Element distribution mappings of TiO_2/CdS micros submarine and the corresponding atomic percentage (at%).

construction of the TiO_2/CdS heterojunction largely improves the visible-light activity and carrier separation efficiency. On the other hand, the etching of the ZnO core has significantly reduced the mass of the micros submarines, which makes the

driven force from weak light enough to propel the motion. When the micros submarines are exposed to the external visible light, they exhibited much faster directional motion. The average velocity was calculated from more than 50 micromotors

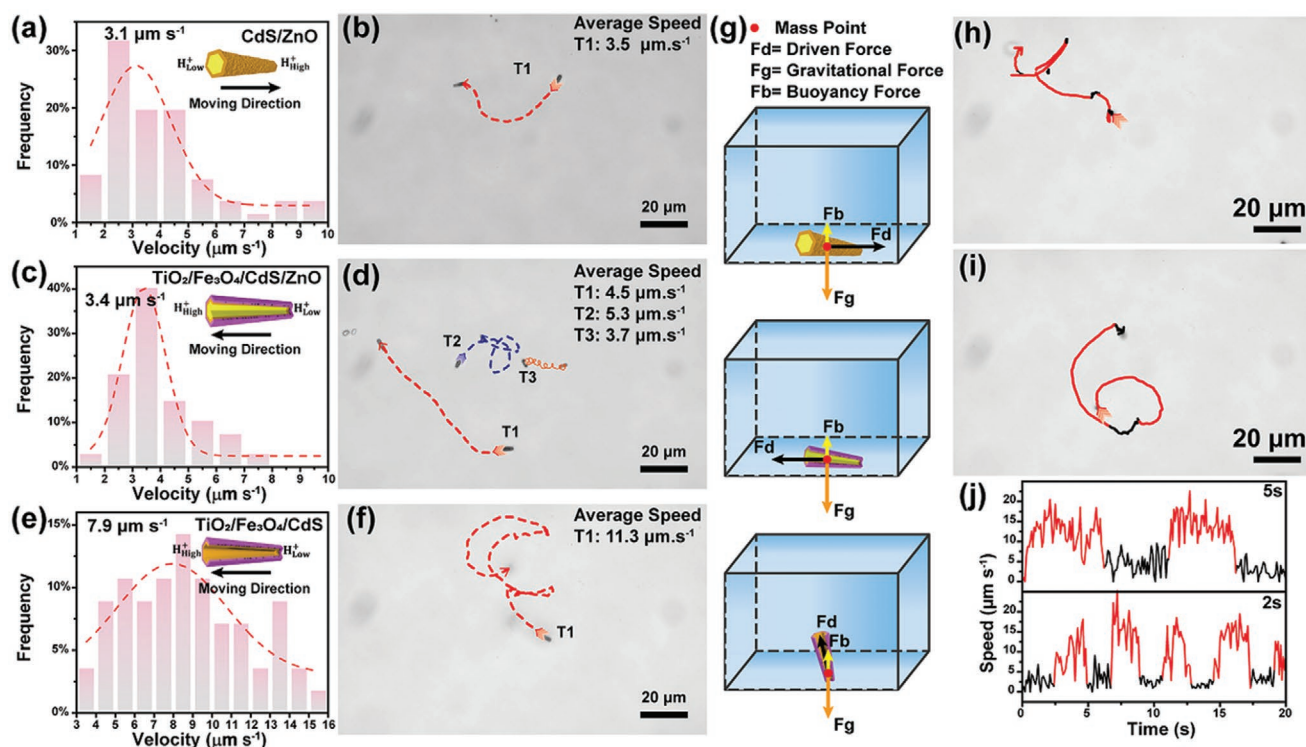


Figure 2. Motion analysis of CdS-based micromotors and proposed mechanisms. The velocity distribution of a) CdS/ZnO micromotors, c) $\text{TiO}_2/\text{Fe}_3\text{O}_4/\text{CdS}/\text{ZnO}$ micromotors, and e) $\text{TiO}_2/\text{Fe}_3\text{O}_4/\text{CdS}$ micros submarines. Insets are the corresponding schematic diagrams of micromotors as well as the motion mechanisms. The representative motion trajectories and the average velocities of b) CdS/ZnO micromotors, d) $\text{TiO}_2/\text{Fe}_3\text{O}_4/\text{CdS}/\text{ZnO}$ micromotors, and f) $\text{TiO}_2/\text{Fe}_3\text{O}_4/\text{CdS}$ micros submarines under visible light irradiation taken from Videos S1–S3 (Supporting Information), respectively. g) Force analysis of micromotor in water under buoyancy force (F_b), gravitational force (F_g), and driven force (F_d). The representative visible-light-driven motion trajectories of $\text{TiO}_2/\text{Fe}_3\text{O}_4/\text{CdS}$ micros submarines with h) 2- or i) 5-s intervals and j) their corresponding velocity profiles taken from Video S4 (Supporting Information).

and fitted with a Gaussian function, where CdS/ZnO micromotors swam with an average velocity of $3.1 \mu\text{m s}^{-1}$ (Figure 2a), $\text{TiO}_2/\text{Fe}_3\text{O}_4/\text{CdS}/\text{ZnO}$ micromotors moved with an average velocity of $3.4 \mu\text{m s}^{-1}$ (Figure 2c), and $\text{TiO}_2/\text{Fe}_3\text{O}_4/\text{CdS}$ microsubmarines showed a faster average velocity of $7.9 \mu\text{m s}^{-1}$ (Figure 2e). Furthermore, some $\text{TiO}_2/\text{Fe}_3\text{O}_4/\text{CdS}$ microsubmarines could move with a velocity as fast as $15 \mu\text{m s}^{-1}$, competitive with some Pt-functionalized micromotors under UV light irradiation.^[16] The representative visible-light-driven motion trajectories and their corresponding motion videos are illustrated in Figure 2b,d,f and Videos S1–S3 (Supporting Information).

The diameter of the top end of our hydrothermally grown ZnO microrods is always smaller than their bottom part, which resulted in the same difference in diameter for CdS/ZnO, $\text{TiO}_2/\text{Fe}_3\text{O}_4/\text{CdS}/\text{ZnO}$, and $\text{TiO}_2/\text{Fe}_3\text{O}_4/\text{CdS}$ micromotors. Hence, we could easily distinguish the moving direction based on micromotors' diameter in the recorded videos, i.e., top-end or bottom-end directions. Moreover, it also provides a facile approach to prove the underlying mechanism of light-driven self-propulsion. We observed that the CdS/ZnO micromotors moved along the top-end direction while they swam along the bottom-end direction in the others' case, $\text{TiO}_2/\text{Fe}_3\text{O}_4/\text{CdS}/\text{ZnO}$ micromotors and $\text{TiO}_2/\text{Fe}_3\text{O}_4/\text{CdS}$ microsubmarines (Figure 2). According to the band-edge positions of the photoactive materials (ZnO, CdS, and TiO_2), the decomposition potentials of water to oxygen (O_2) and hydrogen (H_2), and other oxygen-related redox processes (Figure 3a),^[25,32–35] two mechanisms have been potentially considered for our micromotors (Figure 3b). With the formation of CdS-based heterojunction, the photoresponse of as-prepared CdS/ZnO or CdS/ TiO_2 composites will be extended to the visible-light region, and the charge separation efficiency will be boosted. The visible-light-generated electrons (e^-) inject from the CB of CdS into the CB of ZnO or TiO_2 through the interface while the holes (h^+) remain on the VB of CdS. The photo-generated electrons and holes react with water and produce H_2 and O_2 , respectively. On the other hand, a proton (H^+) gradient will be built during the water oxidation reaction at the CdS side and consumption of H^+ at the ZnO or TiO_2 side, resulting in a local electrical field and driving the negatively charged micromotors to move.^[34,36,37] The $\text{TiO}_2/\text{Fe}_3\text{O}_4/\text{CdS}$ micromotors have a zeta potential of -11.8 mV , indicating a negative surface charge. Besides, the experimental observation indicated that $10 \times 10^{-3} \text{ M}$

NaCl could stop the motion of the micromotors. Therefore, it is suggested that self-electrophoresis is likely to be the mechanism.^[9,38] Considering the self-electrophoretic mechanism, we could predict the direction of motion, precisely the same as what we observed in Videos S1–S3 (Supporting Information), and as schematically illustrated in Figure 2a,c,e. We observed that the $\text{TiO}_2/\text{Fe}_3\text{O}_4/\text{CdS}/\text{ZnO}$ micromotors swam along the bottom-end direction (Video S2, Supporting Information, and Figure 2c) as the CB edge of amorphous TiO_2 is a few more negative (0.24 eV) than that of ZnO,^[31] thus the photogenerated electrons are preferably injected into TiO_2 instead of ZnO.

Moreover, a distinct motion behavior was observed for the $\text{TiO}_2/\text{Fe}_3\text{O}_4/\text{CdS}$ microsubmarines. The $\text{TiO}_2/\text{Fe}_3\text{O}_4/\text{CdS}$ microsubmarines could move away from the focus plane, indicating a Z-direction motion (Figure 2f and Video S3, Supporting Information). Owing to their low weight, the gravitational force exerted on the microsubmarines could be balanced by buoyancy and light-induced motion energy. Thanks to the center of mass closer to the bottom side in this one-end open tubular geometry, the microsubmarines could autonomously adjust their swim direction, i.e., tilt from the horizontal plane shown in Figure 2g and exhibit a 6DoF motion behavior. However, because of the heavy mass, the CdS/ZnO and $\text{TiO}_2/\text{Fe}_3\text{O}_4/\text{CdS}/\text{ZnO}$ micromotors exhibited a normal motion behavior like the other reported inorganic semiconductor-based light-driven microsubmarines, settling to the bottom of the vessel and swimming with four degrees of freedom (Figure 2g). Besides, these $\text{TiO}_2/\text{Fe}_3\text{O}_4/\text{CdS}$ microsubmarines evinced a higher light activity, i.e., a directional movement was observed when illuminated by a weak light from the microscope (Video S3, Supporting Information). On/off switch cycling of the visible light exposure with 2-/5-s intervals were presented in Figure 2h,i and Video S4 (Supporting Information), indicating a fast-responsive activation and deactivation of movement. There is a distinct difference in velocity and displacement corresponding to the light on/off switching, as shown in Figure 2j.

2.3. Controllable Rotation and Locomotion

The rotation and locomotion of the $\text{TiO}_2/\text{Fe}_3\text{O}_4/\text{CdS}$ microsubmarines could be controlled by adjusting the external magnetic field generated by a homemade magnetic controller system

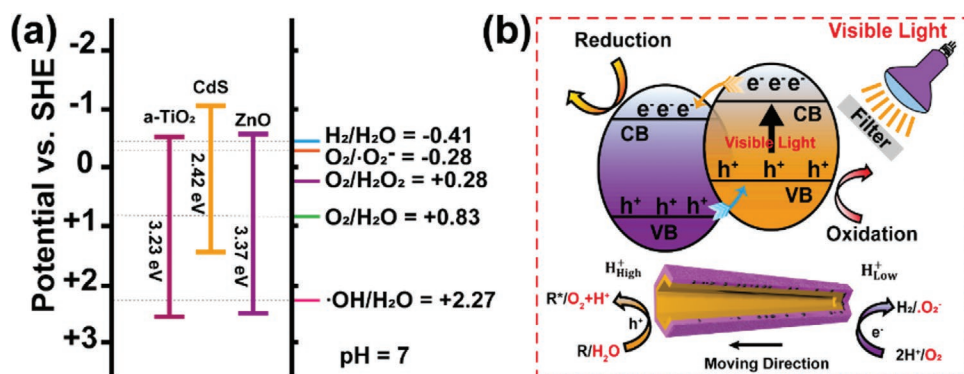


Figure 3. Proposed motion mechanism. a) Band-edge positions of the semiconductors and the corresponding redox potentials for various redox processes occurring at pH 7.^[22] b) Motion mechanisms under visible light. “R” represents the organic molecule before oxidation. “R^{*}” represents the organic molecule after oxidation.

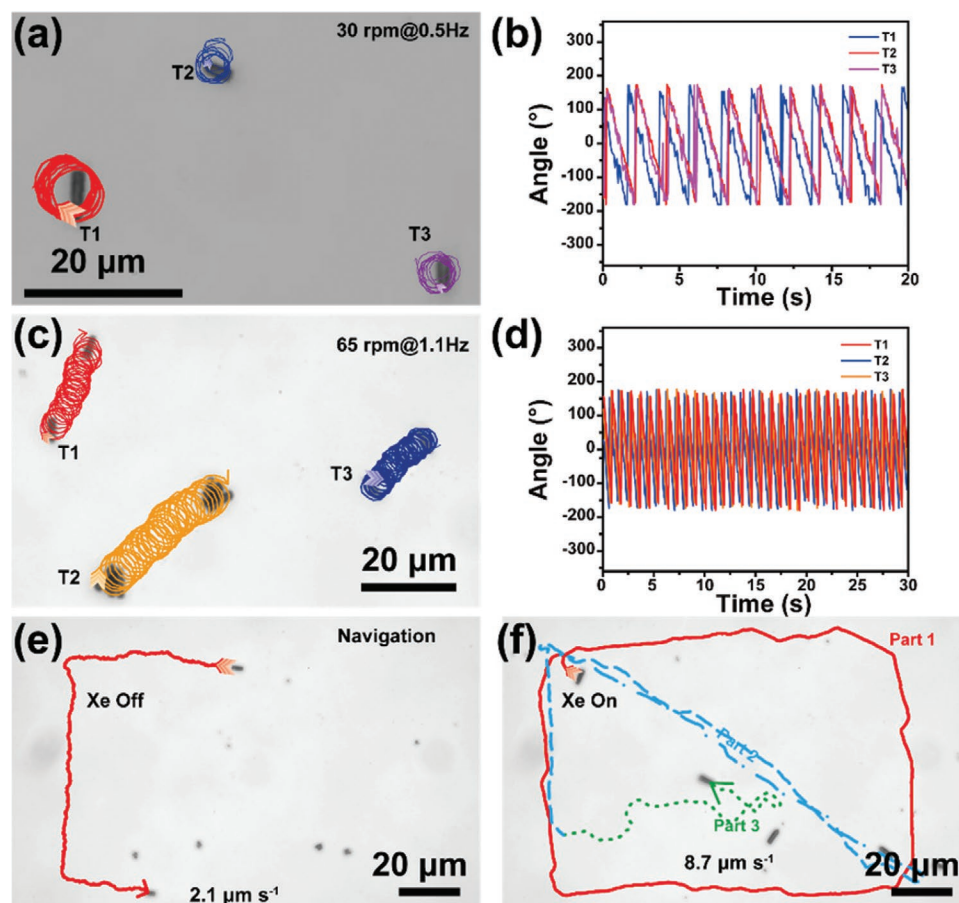


Figure 4. Controllable rotation and directed locomotion of $\text{TiO}_2/\text{Fe}_3\text{O}_4/\text{CdS}$ microsubmarines. The representative rotation trajectories of $\text{TiO}_2/\text{Fe}_3\text{O}_4/\text{CdS}$ microsubmarines under a) 0.5 Hz and c) 1.1 Hz external magnetic field and b, d) their corresponding rotating analysis, i.e., angle versus time, taken from Video S5 (Supporting Information). The magnetic navigation trajectories of $\text{TiO}_2/\text{Fe}_3\text{O}_4/\text{CdS}$ microsubmarines under the external magnetic field in the e) absence/f) presence of the external visible light, taken from Video S6 (Supporting Information).

(Supporting Information). **Figure 4a–d** and Video S5 (Supporting Information) show a typical controllable rotation of the $\text{TiO}_2/\text{Fe}_3\text{O}_4/\text{CdS}$ microsubmarines by adjusting the frequency of the external rotating magnetic field. The $\text{TiO}_2/\text{Fe}_3\text{O}_4/\text{CdS}$ microsubmarines rotated at an expected average speed of 30 and 65 rpm in a 0.5 and 1.1 Hz magnetic field. In addition to the controllable rotation, the $\text{TiO}_2/\text{Fe}_3\text{O}_4/\text{CdS}$ microsubmarines could be manipulated with controllable locomotion under the applied magnetic field in the absence/presence of external visible light, which allows them to travel in a confined space and complete particular tasks. In the absence of external visible light, the $\text{TiO}_2/\text{Fe}_3\text{O}_4/\text{CdS}$ microsubmarines slowly swam under the control of an external magnetic field ($2.1 \mu\text{m s}^{-1}$), with a straight motion and turning (Figure 4e and Video S6, Supporting Information). The resistance of water and weak magnetic force limited the moving ability. In some cases, the micromotors are struck at one position without displacement but only show a response when changing the magnetic direction. With the introduction of external visible light, the $\text{TiO}_2/\text{Fe}_3\text{O}_4/\text{CdS}$ microsubmarines presented a fourfold increase in the motion capability, with an average velocity of $8.7 \mu\text{m s}^{-1}$ (Figure 4f and Video S6, Supporting Information). A particular proof-of-concept task was designed to prove the manipulation of the

$\text{TiO}_2/\text{Fe}_3\text{O}_4/\text{CdS}$ microsubmarines in a confined space by the magnetic field (Figure 4f). At the beginning of the motion, the $\text{TiO}_2/\text{Fe}_3\text{O}_4/\text{CdS}$ microsubmarines swam following a present trajectory of a rectangular shape (solid red line, part 1). Then we controlled the $\text{TiO}_2/\text{Fe}_3\text{O}_4/\text{CdS}$ microsubmarines with a diagonal motion (blue dashed line, part 2). Finally, an ultrasensitive magnetic response was presented (green dotted line, part 3). The microsubmarines responded quickly to the changes in magnetic field orientation.

2.4. Explosive Compound Degradation by CdS-Based Microspheres

Under suitable light stimulation, electron–hole pairs are generated and migrate to the surface of semiconductors, which can produce various reactive species upon interaction with water, yielding hydroxyl ($\cdot\text{OH}$) radical, superoxide ($\cdot\text{O}_2^-$) radical, and hole (h^+) for the degradation of pollutants.^[39] Together with the motion enhanced fluid mixing, these CdS-based micromotors could be used for potential national security (explosive compounds, e.g., picric acid, PA) and environmental application (organic dyes, e.g., methyl orange, MO). Prior to the light

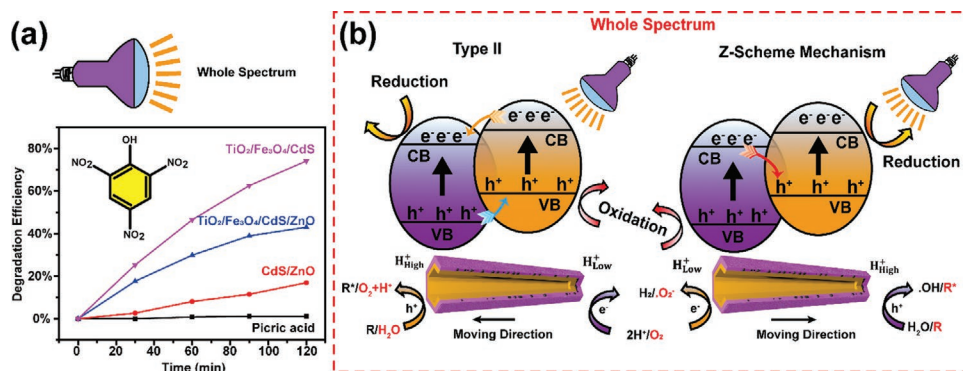


Figure 5. Photodegradation performance and proposed mechanisms under whole-spectrum light (visible light + UV light). a) Degradation efficiency of the micromotors for PA. b) Proposed mechanisms for motion and photodegradation of PA.

irradiation, the micromotors were mixed with the aqueous solution of the targeted pollutant in the dark for more than 1 h to reach the adsorption–desorption equilibrium. The micromotors are collected and separated from the solution through centrifugation or with a magnet. As shown in **Figure 5a** and **Figure S7** (Supporting Information), the photolysis of PA and MO molecules could be neglected; both compounds are stable under visible and UV light irradiation. More motion experiments were performed to pre-confirm the motion capability of micromotors in various condition, where the TiO₂/Fe₃O₄/CdS microsubmarines evinced similar motion behavior in aqueous solutions of either MO or PA under visible light irradiation as well as in pure water under UV light irradiation, as shown in **Videos S7** and **S8** (Supporting Information).

Under visible light illumination, the CdS/ZnO and TiO₂/Fe₃O₄/CdS/ZnO micromotors exhibited low photocatalytic activity for the MO degradation, which only achieved 15% and 20% degradation within 2 h (**Figure 6a**, Supporting Information). In contrast, the TiO₂/Fe₃O₄/CdS microsubmarines exhibited an enhanced photocatalytic performance for the MO degradation with the highest photocatalytic activity of 34% during the same time, almost double compared with that of the CdS/ZnO micromotors (**Figure S7a**, Supporting Information). To our surprise, all the micromotors are ineffective in photocatalytic degradation of PA under visible light irradiation (**Figure S7b**, Supporting Information). We presume that the degradation of PA requires the presence of stronger oxidative species, i.e., hydroxyl radical,^[40] which could not be produced by our CdS-based micromotors under visible light irradiation. All the CdS-based micromotors exhibited significantly enhanced photocatalytic degradation performance for both MO and PA (**Figure 5a** and **Figure S7c**, Supporting Information) under whole-spectrum light irradiation compared to that only under visible light irradiation. The CdS/ZnO and TiO₂/Fe₃O₄/CdS/ZnO micromotors showed a MO degradation efficiency of 22% and 57%, respectively. The corresponding degradation efficiency for TiO₂/Fe₃O₄/CdS reached 84% within 2 h, which is 5.6 times better than that of CdS/ZnO and 2.5 times more than that of TiO₂/Fe₃O₄/CdS micromotors in the visible light region, respectively. More importantly, the TiO₂/Fe₃O₄/CdS microsubmarines presented a distinct PA degradation efficiency under UV light irradiation, with an efficiency of 74% within 2 h, which is four and two times higher than that of CdS/ZnO and TiO₂/

Fe₃O₄/CdS/ZnO micromotors, respectively. These results indicated that both the surface coating of the amorphous TiO₂ layer and the 6DoF movement of TiO₂/Fe₃O₄/CdS microsubmarines could improve the degradation performance. Moreover, UV light irradiation is an essential requirement for PA degradation.

Based on the results mentioned above, the theoretical band positions of CdS, α -TiO₂, and ZnO, and the redox potentials of water decomposition reactions (**Figure 3a**),^[25,32–35] possible mechanisms were proposed for the explanation of the enhanced photocatalytic activity of micromotors for MO and PA degradation under visible and UV light irradiation. As shown in **Figure 3b**, when the micromotors were exposed to the visible light, electron–hole pairs could be activated in CdS according to the narrow bandgap of 2.42 eV. Electrons were excited from the VB to the CB. Then the photogenerated electrons migrated from the CB of CdS to the CB of ZnO due to the CB edge potential of CdS being more negative (ZnO < CdS) while the holes remain in the VB of CdS.^[35] In the presence of the α -TiO₂ layer, the electrons preferably migrate to the CB of α -TiO₂ where the CB edge potential is 0.24 eV more negative than ZnO.^[28] The photogenerated electrons in the CB of ZnO or α -TiO₂ could directly react with surface adsorbed oxygen (O₂) and produce superoxide radicals (O₂⁻/O₂⁻ = -0.28 eV at pH 7).^[25] Due to the VB edge position of CdS more negative than the standard redox potential of [•]OH ([•]OH/H₂O = 2.27 eV), the holes could not react with water and generate [•]OH radical. However, h⁺ can directly interact with organic molecules (R). Therefore, it is inferred that h⁺ and [•]O₂⁻ are the primary active species responsible for the photocatalytic degradation. Moreover, the degradation of PA requires stronger oxidative species, e.g., the hydroxyl ([•]OH) radical.^[40] Under the whole-spectrum light irradiation, the electron–hole pairs were generated on the ZnO or TiO₂ side. Conventionally, typical Type-II and direct Z-scheme heterojunction are widely used as an explanation of the electron–hole transport (**Figure 5b**). In general, the photogenerated electrons left in the VB of ZnO or TiO₂ and corresponding holes tend to transfer the VB of CdS, which suppresses the [•]OH radical production ability (**Figure 5b**, Type II). However, from the experimental results, the micromotors' photodegradation ability under the whole-spectrum light irradiation is much stronger than that only under the visible light, and the stable PA is also degraded with high efficiency.

It is suggested that more active species, such as $\cdot\text{OH}$ radical, should be involved in the reaction. This conflicting phenomenon has been observed in some other reports^[41] while some give misleading or ambiguous explanations.^[42–45] Three possible mechanisms were proposed to explain the production of the $\cdot\text{OH}$ radical. Concerning the direct Z-scheme mechanism (Figure 5b, Z-scheme mechanism), electrons in the CB of ZnO or TiO_2 and holes in the VB of CdS recombine directly, resulting in the preservation of electrons and holes with better reductive and oxidative abilities.^[46] The Z-scheme dominant heterojunction structure could produce $\cdot\text{OH}$ radicals by the holes in the CB of ZnO or TiO_2 . This mechanism perfectly explains the significant difference in photocatalytic degradation performance under visible light and UV light. However, it is not consistent with the motion direction we observed, where the $\text{TiO}_2/\text{Fe}_3\text{O}_4/\text{CdS}$ microsubmarines swim following the same direction under UV light and visible light (bottom-end direction, Video S8, Supporting Information). If the direct Z-scheme mechanism is responsible for the production of $\cdot\text{OH}$ radical under the UV region, the $\text{TiO}_2/\text{Fe}_3\text{O}_4/\text{CdS}$ microsubmarines were supposed to show opposite moving direction compared with that under visible illustration. Another possible mechanism is that the $\cdot\text{O}_2^-$ radical could be consumed to produce hydrogen peroxide (H_2O_2).^[47–49] The subsequent decomposition of H_2O_2 under UV light generates the $\cdot\text{OH}$ radicals.^[50,51] The third explanation is that the isolated TiO_2 or ZnO, which are not involved in the formation of the heterojunction structure, produce $\cdot\text{OH}$ radical under UV irradiation, enhance the catalytic performance, and degrade the PA molecules. Based on the experimental results and theoretical studies, we believe the third mechanism may play a dominant role in boosting the degradation performance.

3. Conclusion

Herein, we developed a facile methodology to design visible-light-driven CdS-based microsubmarines with 6DoF motion behavior built on vertically grown ZnO arrays to enhance explosive compounds' degradation performance. All the CdS-based micromotors, i.e., CdS/ZnO, $\text{TiO}_2/\text{Fe}_3\text{O}_4/\text{CdS}/\text{ZnO}$, and $\text{TiO}_2/\text{Fe}_3\text{O}_4/\text{CdS}$, exhibited a directional movement under visible-light illustration without any external fuels. Significantly, the tubular $\text{TiO}_2/\text{Fe}_3\text{O}_4/\text{CdS}$ microsubmarines showed a 6DoF motion behavior and the fastest velocity, significantly enhancing their motion-induced fluid mixing capability. The $\text{TiO}_2/\text{Fe}_3\text{O}_4/\text{CdS}$ microsubmarines demonstrated a controllable rotation and directional locomotion under an external magnetic field. The composition (ZnO or TiO_2) and structure differences (diameter difference between the two ends of micromotors) were used to study the visible-light-driven motion mechanism according to carriers' transportation in heterojunction and motion direction. It is suggested that self-photophoresis is likely to be the mechanism where a proton gradient over the micromotor is generated under the light illustration. Furthermore, the CdS-based micromotors were used for the degradation of PA and MO. The $\text{TiO}_2/\text{Fe}_3\text{O}_4/\text{CdS}$ microsubmarines exhibited the best photocatalytic activity under the whole-spectrum light for PA degradation (74%), which is four times better than

that of CdS/ZnO micromotors under the same condition due to the versatility of 6DoF movement, the surface coating of the amorphous TiO_2 layer, and UV light. Due to the existence of isolated TiO_2 or ZnO, which is not involved in formation of the heterojunction structure, the generation of $\cdot\text{OH}$ radicals under UV irradiation could enhance the catalytic performance and degrade the explosive PA molecules. The photodegradation mechanism was analyzed based on the photoactive materials' band-edge positions compared with the chemical reduction potentials of water decomposition reactions under visible and UV light irradiation. Our work contributes to an alternative way of understanding the self-photophoresis motion mechanism and optimizes light-active micromotor design for potential national security and environmental application, hydrogen evolution, and target cargo delivery.

4. Experimental Section

Chemical: The chemicals used in the experiments were zinc nitrate hexahydrate ($\text{Zn}(\text{NO}_3)_2 \cdot 6\text{H}_2\text{O}$, $\geq 98\%$, Strem Chemicals), hexamethylenetetramine ($\text{C}_6\text{H}_{12}\text{N}_4$, HMTA, $\geq 99.5\%$, Penta), thioacetamide ($\text{C}_2\text{H}_5\text{NS}$, TAA, $\geq 98\%$, Sigma-Aldrich), chromium nitrate nonahydrate ($\text{Cr}(\text{NO}_3)_3 \cdot 9\text{H}_2\text{O}$, 99%, Sigma-Aldrich), iron chloride hexahydrate ($\text{FeCl}_3 \cdot 6\text{H}_2\text{O}$, $\geq 99.9\%$, VWR), ammonium iron(II) sulfate hexahydrate ($(\text{NH}_4)_2\text{Fe}(\text{SO}_4)_2 \cdot 6\text{H}_2\text{O}$, $\geq 98.3\%$, Sigma-Aldrich), sodium citrate tribasic dihydrate ($\text{Na}_3\text{C}_6\text{H}_5\text{O}_7 \cdot 2\text{H}_2\text{O}$, $\geq 99.0\%$, Sigma-Aldrich), hydrochloric acid (HCl, 35%, Penta), titanium chloride (TiCl_4 , 99.9%, Sigma Aldrich), methyl orange (4-(4-(dimethylamino)phenylazo) benzenesulfonic acid sodium salt ($\text{C}_{14}\text{H}_{14}\text{N}_3\text{SO}_3\text{Na}$, ACS reagent, dye content 85%, Sigma-Aldrich), and picric acid (2,4,6-trinitrophenol ($\text{O}_2\text{N})_3\text{C}_6\text{H}_2\text{OH}$, HPLC grade, $\geq 98\%$, Sigma-Aldrich). Deionized (DI, 18.2 M Ω cm at 25 °C) water was used in all experiments. Silicon wafer (<100) was purchased from University Wafers.

Hydrothermal Growth of ZnO Arrays on the Silicon Wafer: Si (100) wafer was chosen as the substrate without further treatment. ZnO nanorods were grown on the substrate by the hydrothermal method.^[16] First, a silicon wafer was smooth-side (up-side) down immersed in a sealed polytetrafluoroethylene (PTFE) container (100 mL), with 60 mL ZnO precursor solution containing 0.05 M $\text{Zn}(\text{NO}_3)_2 \cdot 6\text{H}_2\text{O}$ and 0.05 M hexamethylenetetramine (HMTA). The hydrothermal reaction was performed at 90 °C for 4 h. Then the autoclave was fast cooling down to room temperature by water. Subsequently, the substrate was washed repeatedly with deionized water to remove the free ZnO on the surface and backside and dried in air.

Preparation of CdS/ZnO Core-Shell Structured Nanorods Array: Core-shell structured CdS-ZnO nanorods array was synthesized via a simple chemical bath deposition process. First, the silicon wafer with ZnO arrays was upside down immersed in an aqueous solution containing 1 mL of TAA (100×10^{-3} M, EtOH) and 10 mL of water to form a ZnS shell on the surface at 65 °C for 60 min. The aqueous solution was subsequently replaced with 1 mL of CdCl_2 (100×10^{-3} M), 9 mL of water, and 1 mL of ethanol and heated at 65 °C for an additional 60 min. Yellow CdS shell assembled on the surface of the ZnO nanorods. The CdS/ZnO arrays were repeatedly washed with deionized water to remove the residual chemicals. Finally, CdS/ZnO core-shell arrays were annealed in argon at 550 °C for 30 min to improve the interfaces between ZnO and CdS as well as the structure of the CdS shells.^[52]

Surface Decoration of Fe_3O_4 NPs: The citrate-functionalized Fe_3O_4 NPs were prepared using the reported modified method.^[53] 1 mL of Fe_3O_4 NPs suspension (1.925 mg mL $^{-1}$) was diluted with 5 mL of water and 5 mL of ethanol. Then silicon wafer with the CdS/ZnO rods was immersed into the above-mentioned solution and incubated for 1 d with slight shaking. Subsequently, the residual Fe_3O_4 NPs were removed by washing with deionized water, and the $\text{Fe}_3\text{O}_4/\text{CdS}/\text{ZnO}$ array was dried at room temperature.

ALD Deposition of TiO₂ Layers: The TiO₂ layers were deposited on the surface of the silicon wafer with Fe₃O₄/CdS/ZnO array using a PICOSUN R-200 Advanced ALD system with TiCl₄ and H₂O as the precursors and 6N nitrogen as the carrier gas. The substrate was heated to 300 °C. The pressure in the deposition chamber was 500 Pa. TiO₂ ALD sequence of TiCl₄ exposure (0.2 s)–N₂ purging (5 s)–H₂O exposure (1 s)–N₂ purging (10 s) was repeated 1000 times at 300 °C.

Detachment of Micromotors: CdS/ZnO and TiO₂/Fe₃O₄/CdS/ZnO motors were detached from the silicon substrate by scraping and collected by centrifugation or magnet. The TiO₂/Fe₃O₄/CdS micromotors were prepared by etching the ZnO core from the TiO₂/Fe₃O₄/CdS/ZnO using 2 mL of HCl (pH = 2) (water:EtOH = 50:50 vol%) with slight shaking for 1 d. Subsequently, the TiO₂/Fe₃O₄/CdS motors were washed with DI water three times and collected using a magnet.

Characterization: Field-emission scanning electron microscopy (Maia 3, Tescan) coupled with energy-dispersive spectrometer (Oxford instrument) was used to obtain the SEM (5 kV) and STEM (30 kV) images of the morphology and EDS mapping (10 kV, X-Max 150 and X-Extreme). X-ray diffraction result was performed using Bruker D2 Phaser system with a Cu X-ray source. Zeta-potential measurements were performed on a Malvern Zetasizer Nano ZS. The suspension used for motion analysis was directly used without further treatment.

Motion Record and Track: Light-Driven Motion: About 3 μL of an aqueous solution containing the motors was dropped on a glass slide, followed by the addition of 50 μL of DI water. An optical microscope (Olympus IX 73), coupled with a 50× objective, using a high-speed camera (Basler ace acA1920-155uc) along with pylon view software to record videos (1920 px × 1200 px, 30 fps, 10.3617 pixel μm⁻¹) was used. An external mercury arc lamp (X-Cite 120 Q, 120 W) was used as a light source. A visible light filter cube (2) was used to remove the wavelengths below 400 nm to obtain a visible light with a power density of 2.5 W cm⁻². Another low pass filter cube (1) was used to obtain UV light.

Magnetic Manipulation: A homemade magnetic controller system with two perpendicular coil pairs was attached to a microscope table, generating a horizontal or vertical rotating magnetic field. The 3D-printed polylactic acid (PLA) skeleton was used to hold the coil components and assembled to the microscope table. A particular hand shank connecting with the coil pairs was used to select the different models (rotation or navigation) and control the movement direction by a particular power supply, with a microcontroller which could adjust two power bidirectional current source. The rotation experiment was carried out at 0.5 and 1.1 Hz. The navigation experiment was performed with a 6 A current in X- or Y-direction. The videos were taken by a Basler acA1920-155uc camera at 30 fps mounted on the Olympus IX 73 microscope equipped with a 50× objective. Image-pro premier 9.1 software was used for the trajectories tracking and velocity analysis of the motors in auto-track and manual track mode.

Photocatalytic Degradation: CdS/ZnO, TiO₂/Fe₃O₄/CdS/ZnO, and TiO₂/Fe₃O₄/CdS micromotors were used for photocatalytic activity assessment. Methyl orange (MO, 5 × 10⁻⁶ M) and picric acid (PA, 5 × 10⁻⁶ M) were used as the targeted dyes under whole-spectrum light and visible light. The motors from the same area of the silicon substrate (1 × 2 cm²) were mixed with 2 mL of the above dye aqueous solution. The light source was simulated using a UV lamp (Ultra-Vitalux 300 W 230 V AC T758, Osram). The mixture was placed in a glass bottle (diameter 1 cm) above the light source at the 40 cm distance without stirring, and a polyester UV filter sheet (Edmund Optics) was applied to remove wavelength radiation below 400 nm. Before the light irradiation, the mixture was standing for 10 min to ensure that the motors precipitated to the bottom. 0.3 mL of the mixture was taken out every 30 min, and the degradation test was terminated after 2 h. The dye concentration was determined using a UV-vis spectrophotometer (Multiskan Sky, Thermal Scientific) after separating the motors from the mixture by centrifugation or magnet. The degradation efficiency (%) was determined based on Equation (1)

$$\text{Degradation efficiency (\%)} = (1 - C_i/C_0) \times 100\% \quad (1)$$

where i is the reaction time, C_i is the concentration of residual picric after micromotor treatment, and C_0 is the initial concentration of dye used in the degradation test. The degradation efficiency was measured at 354 nm peak of picric acid and 464 nm of methyl orange.

Supporting Information

Supporting Information is available from the Wiley Online Library or from the author.

Acknowledgements

This work was supported by the project Advanced Functional Nanorobots (Reg. No. CZ.02.1.01/0.0/0.0/15_003/0000444 financed by the EFRR). M.P. was supported by Ministry of Education, Youth and Sports (Czech Republic) grant LL2002 under ERC CZ program.

Conflict of Interest

The authors declare no conflict of interest.

Data Availability Statement

Research data are not shared.

Keywords

explosive decontamination, micromotor, six degrees of freedom, visible-light-driven, water fuel

Received: January 16, 2021

Revised: March 13, 2021

Published online: May 4, 2021

- [1] Y. Y. Sun, Y. Liu, B. Song, H. Zhang, R. M. Duan, D. F. Zhang, B. Dong, *Adv. Mater. Interfaces* **2019**, *6*, 1801965.
- [2] H. Eskandarloo, A. Kierulf, A. Abbaspourrad, *Nanoscale* **2017**, *9*, 12218.
- [3] J. Parmar, D. Vilela, K. Villa, J. Wang, S. Sanchez, *J. Am. Chem. Soc.* **2018**, *140*, 9317.
- [4] Y. Ying, M. Pumera, *Chem* **2019**, *25*, 106.
- [5] K. Villa, M. Pumera, *Chem. Soc. Rev.* **2019**, *48*, 4966.
- [6] H. Sipova-Jungova, D. Andren, S. Jones, M. Kall, *Chem. Rev.* **2020**, *120*, 269.
- [7] W. P. He, J. Frueh, N. Hu, L. P. Liu, M. Y. Gai, Q. He, *Adv. Sci.* **2016**, *3*, 1600206.
- [8] a) W. P. He, J. Frueh, Z. W. Wu, Q. He, *Langmuir* **2016**, *32*, 3637; b) S. Rutkowski, T. Si, M. Gai, M. Sun, J. Frueh, Q. He, *J. Colloid Interface Sci.* **2019**, *25*, 752.
- [9] D. Zhou, R. Zhuang, X. Chang, L. Li, *Research* **2020**, *2020*, 6821595.
- [10] L. L. Xu, F. Z. Mou, H. T. Gong, M. Luo, J. G. Guan, *Chem. Soc. Rev.* **2017**, *46*, 6905.
- [11] R. F. Dong, Q. L. Zhang, W. Gao, A. Pei, B. Y. Ren, *ACS Nano* **2016**, *10*, 839.
- [12] R. Dong, Y. Hu, Y. Wu, W. Gao, B. Ren, Q. Wang, Y. Cai, *J. Am. Chem. Soc.* **2017**, *139*, 1722.
- [13] K. Villa, F. Novotny, J. Zelenka, M. P. Browne, T. Ruml, M. Pumera, *ACS Nano* **2019**, *13*, 8135.

- [14] D. K. Zhou, Y. G. C. Li, P. T. Xu, N. S. McCool, L. Q. Li, W. Wang, T. E. Mallouk, *Nanoscale* **2017**, *9*, 75.
- [15] A. M. Pourrahimi, K. Villa, C. L. M. Palenzuela, Y. L. Ying, Z. Sofer, M. Pumera, *Adv. Funct. Mater.* **2019**, *29*, 1808678.
- [16] Y. L. Ying, A. M. Pourrahimi, C. L. Manzanara-Palenzuela, F. Novotny, Z. Sofer, M. Pumera, *Small* **2020**, *16*, 1902944.
- [17] S. N. Du, H. G. Wang, C. Zhou, W. Wang, Z. X. Zhang, *J. Am. Chem. Soc.* **2020**, *142*, 2213.
- [18] K. Villa, C. L. M. Palenzuela, Z. Sofer, S. Matejkova, M. Pumera, *ACS Nano* **2018**, *12*, 12482.
- [19] V. Sridhar, B. W. Park, S. R. Guo, P. A. van Aken, M. Sitti, *ACS Appl. Mater. Interfaces* **2020**, *12*, 24149.
- [20] X. Wang, L. Baraban, A. Nguyen, J. Ge, V. R. Misko, J. Tempere, F. Nori, P. Formanek, T. Huang, G. Cuniberti, J. Fassbender, D. Makarov, *Small* **2018**, *14*, 1803613.
- [21] D. O. Adekoya, M. Tahir, N. A. S. Amin, *J. CO₂ Util.* **2017**, *18*, 261.
- [22] R. M. Goody, Y. L. Yung, *Atmospheric Radiation: Theoretical Basis*, Oxford University Press, Oxford **1995**.
- [23] X. He, R. Buchel, R. Figi, Y. C. Zhang, Y. Bahk, J. Ma, J. Wang, *Chemosphere* **2019**, *219*, 427.
- [24] A. M. Pourrahimi, K. Villa, Y. L. Ying, Z. Sofer, M. Pumera, *ACS Appl. Mater. Interfaces* **2018**, *10*, 42688.
- [25] A. Fujishima, T. N. Rao, D. A. Tryk, *J. Photochem. Photobiol., C* **2000**, *1*, 1.
- [26] C. Venkatarreddy, N. Bandaru, I. N. Reddy, J. Shim, K. Yoo, *Mater. Sci. Eng., B* **2018**, *232*, 68.
- [27] J. M. Xu, H. X. Sang, X. T. Wang, K. Wang, *Dalton Trans.* **2015**, *44*, 9528.
- [28] Y. X. Yu, W. X. Ouyang, Z. T. Liao, B. B. Du, W. D. Zhang, *ACS Appl. Mater. Interfaces* **2014**, *6*, 8467.
- [29] Y. Ying, T. Song, H. Huang, X. Peng, *Appl. Phys. A* **2013**, *110*, 351.
- [30] Y. T. Guo, D. C. Wang, J. A. Li, Y. Y. Sun, M. T. Li, H. Zhang, R. M. Duan, D. F. Zhang, B. Song, B. Dong, *J. Mater. Chem. C* **2019**, *7*, 2299.
- [31] S. S. Xiao, L. Zhao, X. N. Leng, X. Y. Lang, J. S. Lian, *Appl. Surf. Sci.* **2014**, *299*, 97.
- [32] S. Tso, W. S. Li, B. H. Wu, L. J. Chen, *Nano Energy* **2018**, *43*, 270.
- [33] L. X. Zheng, F. Teng, X. Y. Ye, H. J. Zheng, X. S. Fang, *Adv. Energy Mater.* **2020**, *10*, 1902355.
- [34] J. S. Luo, L. Ma, T. C. He, C. F. Ng, S. J. Wang, H. D. Sun, H. J. Fan, *J. Phys. Chem. C* **2012**, *116*, 11956.
- [35] Z. M. Bai, X. Q. Yan, Y. Li, Z. Kang, S. Y. Cao, Y. Zhang, *Adv. Energy Mater.* **2016**, *6*, 1501459.
- [36] B. H. Dai, J. Z. Wang, Z. Xiong, X. J. Zhan, W. Dai, C. C. Li, S. P. Feng, J. Y. Tang, *Nat. Nanotechnol.* **2016**, *11*, 1087.
- [37] L. Kong, C. C. Mayorga-Martinez, J. G. Guan, M. Pumera, *Small* **2020**, *16*, 1903179.
- [38] X. Zhan, J. Wang, Z. Xiong, X. Zhang, Y. Zhou, J. Zheng, J. Chen, S. P. Feng, J. Tang, *Nat. Commun.* **2019**, *10*, 3921.
- [39] K. L. Lv, Y. M. Xu, *J. Phys. Chem. B* **2006**, *110*, 6204.
- [40] B. H. Bielski, D. E. Cabelli, *Active Oxygen in Chemistry*, Springer, Berlin **1995**, pp. 66–104.
- [41] V. Rajendran, M. Lehnig, C. M. Niemeyer, *J. Mater. Chem.* **2009**, *19*, 6348.
- [42] H. Wang, Q. Xu, X. Zheng, W. Q. Han, J. T. Zheng, B. Jiang, Q. Z. Xue, M. B. Wu, *J. Nanopart. Res.* **2014**, *16*, 2794.
- [43] F. Xu, Y. F. Yuan, H. J. Han, D. P. Wu, Z. Y. Gao, K. Jjiang, *CrystEngComm* **2012**, *14*, 3615.
- [44] C. H. Chen, Z. C. Li, H. N. Lin, G. J. Wang, J. C. Liao, M. Y. Li, S. S. Lv, W. Li, *Dalton Trans.* **2016**, *45*, 3750.
- [45] R. C. Pawar, C. S. Lee, *Appl. Catal., B* **2014**, *144*, 57.
- [46] S. Wang, B. C. Zhu, M. J. Liu, L. Y. Zhang, J. G. Yu, M. H. Zhou, *Appl. Catal., B* **2019**, *243*, 19.
- [47] M. Buchalska, M. Kobielski, A. Matuszek, M. Pacia, S. Wojtyła, W. Macyk, *ACS Catal.* **2015**, *5*, 7424.
- [48] M. Hayyan, M. A. Hashim, I. M. AlNashef, *Chem. Rev.* **2016**, *116*, 3029.
- [49] Y. Nosaka, S. Takahashi, H. Sakamoto, A. Y. Nosaka, *J. Phys. Chem. C* **2011**, *115*, 21283.
- [50] E. Simonenko, A. Gomonov, N. Rolle, L. Molodkina, *Proc. Eng.* **2015**, *117*, 337.
- [51] A. Y. Meng, B. C. Zhu, B. Zhong, L. Y. Zhang, B. Cheng, *Appl. Surf. Sci.* **2017**, *422*, 518.
- [52] Q. Yang, Y. L. Li, Z. G. Hu, Z. H. Duan, P. P. Liang, J. Sun, N. Xu, J. D. Wu, *Opt. Express* **2014**, *22*, 8617.
- [53] Y. L. Ying, A. M. Pourrahimi, Z. Sofer, S. Matejkova, M. Pumera, *ACS Nano* **2019**, *13*, 11477.